ChemComm

COMMUNICATION

View Article Online
View Journal | View Issue

Cite this: *Chem. Commun.*, 2025, **61**, 14919

Received 7th July 2025,
Accepted 15th August 2025

DOI: 10.1039/d5cc03808a

rsc.li/chemcomm

Multi-modal impedance and X-ray characterization enables simultaneous detection of bulk and interfacial crystallization

Nikolaus Doppelhammer, *[ab] Daniel Spira, [c] Anjul Rais, [b] Dries Vandenabeele, [b] Wauter Wangermez, [b] Charles McMonagle, [d] Dmitry Chernyshov [d] and Eric Breynaert *[ab]

A multi-modal platform enabling simultaneous impedance spectroscopy and X-ray scattering is presented. When applied to zeolite crystallization, four-electrode impedance measurements reliably track bulk crystallization kinetics in agreement with X-ray diffraction, while two-electrode impedance data reveal artefacts from electrode passivation.

The synthesis of materials often sensitively depends on chemical and physical conditions. Prominent examples include the synthesis of nanoparticles and nanocrystals,[1–5] polymers,[6] quantum nanodots,[7] thin films,[8,9] and porous materials.[10,11] In all cases, minor impurities or subtle variations in sample composition, temperature, and pressure can drastically alter the synthesis outcome. In well-controlled cases, such sensitivity can be advantageous to precisely steer kinetics and product properties. Unrecognized effects, however, pose major challenges, specifically when multiple transformation pathways, intermediates or side products are involved. In such cases, characterization employing several complementary diagnostics is indispensable to capture all relevant aspects of a synthesis. However, when diagnostics are physically separated, inconsistencies may arise due to variations in the sample environment (such as geometry, interfaces, and temperature transients or non-uniform temperature fields), calibration errors, or differences in sample handling.

Combining complementary diagnostics in a single sample environment is therefore highly desirable, as it minimizes inconsistencies and improves efficiency by reducing analysis cost and time. However, many standard techniques (*e.g.*, NMR spectroscopy, X-ray methods or electron microscopy) are physically incompatible due to differing requirements for instruments and the sample environment. As a result, they can only be combined virtually, *i.e.*, data are integrated post-measurement rather than acquired simultaneously.

Here, impedance spectroscopy offers a unique and versatile opportunity. Due to its comparatively low experimental complexity, it can be integrated with many other techniques. Impedance spectroscopy probes frequency-dependent electrical and dielectric properties, enabling insights into ionic mobility, phase composition, and interfacial phenomena. This allows correlating results across different measurement platforms using the fingerprint of the impedance data, and it also provides complementary information to structural or compositional data. For example, impedance spectroscopy can detect changes in conductivity or permittivity associated with structural rearrangements, pre-ordering, or meso- and macroscale interfacial phenomena. Such events accompany or precede crystallization, thereby providing insights into nucleation pathways and amorphous-to-crystalline transitions.[12–17]

In this work, an innovative approach integrating two- and four-electrode impedance spectroscopy with simultaneous X-ray characterization, along with temperature monitoring in a microliter-sized sample environment, is presented. The capabilities of the integrated platform are demonstrated in the context of zeolite crystallization, a class of porous materials with high industrial and societal impact.[18–21] Their crystallization pathways and product properties are sensitively influenced by the composition and synthesis conditions (*e.g.*, temperature), often exhibiting a significant degree of variability. This, together with the harsh zeolite synthesis conditions, presents a challenge for consistent experimental characterization.

The cell design for combined impedance and X-ray characterization is illustrated in Fig. 1. A photograph of the full setup and its integration into the BM01 beamline at the European Synchrotron Radiation Facility (Grenoble, France) is shown in Fig. S1 of the SI. The design builds upon an already

[a] *NMRCoRe-NMR/X-Ray platform for Convergence Research, KU Leuven, Leuven 3001, Belgium. E-mail: nikolaus.doppelhammer@kuleuven.be, eric.breynaert@kuleuven.be*
[b] *Centre for Surface Chemistry and Catalysis Characterisation and Application Team (COK-KAT), KU Leuven, Leuven 3001, Belgium*
[c] *Institute for Microelectronics and Microsensors, Johannes Kepler University Linz, Linz 4020, Austria*
[d] *Swiss–Norwegian Beamlines at the European Synchrotron Radiation Facility, 38000 Grenoble, France*

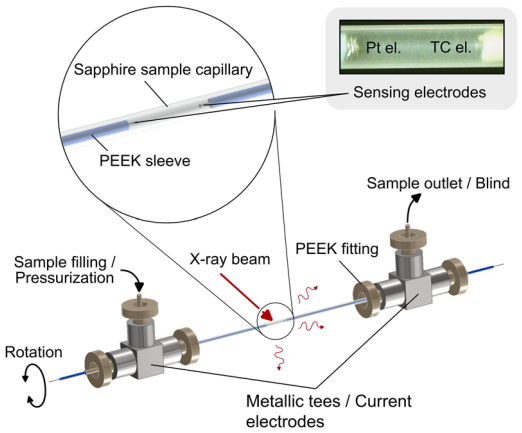

Fig. 1 Sample environment for combined *in situ* electrical impedance and X-ray characterization.

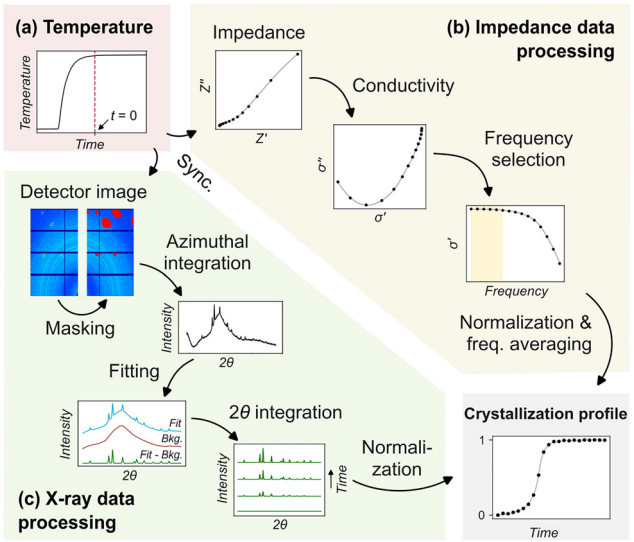

Fig. 2 Data processing workflows for (a) temperature, (b) impedance, and (c) X-ray data, illustrated based on the example of the crystallizing sample containing Cs^+ cations. Additional information on the processing steps is provided in Sections S4 and S5 of the SI.

commissioned high-pressure sample environment featuring a single crystal sapphire capillary.[22] Although sapphire leads to stronger attenuation of X-rays and the single crystalline nature of the capillary produces diffraction spots on the detector image, it was selected for its superior chemical, pressure and temperature resistance as compared to, for example, quartz glass.[23] The dimensions of the capillary (d_i = 1 mm, d_0 = 1.57 mm) ensure compatibility with commercially available polyether ether ketone (PEEK) fittings and tubes. Three-way adapters (“tees”) facilitate sample loading and pressurization, as well as integration of electrodes. A thin spring-wound platinum wire served as one of the two inner electrodes (“Pt el.”; see the inset of Fig. 1), while the sheath of a metal-sheathed thermocouple was used as the second inner electrode (“TC el.”). This way a sample environment is created in which temperature, X-ray characterization and impedance measurements can be performed in a microliter-sized volume (~4 μL). Furthermore, since the tees are in direct contact with the liquid, their design as metallic components allows them to function as outer electrodes in a four-electrode impedance measurement.[24–27] To ensure electrical insulation in the sections between inner and outer electrodes, both the platinum electrode and the thermocouple were housed in PEEK capillary tubes, sealed *via* thermo-compression bonding near the sensing region. The cell was mounted on a custom U-shaped holder, which itself was mounted on a motorized goniometer, enabling axial rotation of the capillary in a large angular range up to 250°. A custom cartridge-based heating system was developed for maintaining a uniform temperature in a large section of the capillary. Fast heat-up times of the sample were achieved by preheating the heater to the target temperature and moving it into the capillary using a motorized linear stage. Further details on the setup are provided in Tables S1.1 and S1.2 of the SI.

To demonstrate the ability of the combined impedance and X-ray platform, crystallization systems in the realm of inorganic zeolite formation were selected. Samples were synthesized using a hydrated silicate ionic liquid (HSIL)-based recipe, explained in detail in previous publications.[28,29] Pure HSILs containing Na^+ or Cs^+ as alkali cations were prepared and mixed with the corresponding alkali metal aluminate solutions to yield synthesis mixtures with composition: 5 $Si(OH)_4$: 0.03 $Al(OH)_3$: 1 MOH : 9 H_2O, where M represents Na or Cs. These alkali metals were selected due to their distinct interactions with aluminosilicate species, which results in different crystallization behavior.[11,30] Temperatures of 120 °C for the Cs-based sample and 140 °C for the Na-based sample were chosen to achieve a reasonable synthesis duration. A constant pressure of 40 bar was applied during the experiments to avoid gas bubble formation. Further details on the sample preparation and the measurements are provided in Section S2 of the SI.

To synchronize impedance, X-ray and temperature measurements, all data were time-stamped and referenced to the point when the thermocouple temperature reached 99% of the set-point value (defined as “t = 0” in Fig. 2(a)). Impedance spectra were consecutively recorded in two- and four-electrode configurations, each in the frequency range from 500 Hz to 500 kHz using an excitation voltage of 300 mV. Switching between the configurations was achieved using a custom relay-based switch (Fig. S3, SI). Recording of an impedance spectrum took approximately 5 s and was triggered simultaneously with X-ray acquisition. In the two-electrode mode, where the sensing electrodes simultaneously serve as the current-carrying electrodes, impedance is influenced by electrode polarization. This effect is particularly severe in highly conductive media and at low measurement frequencies.[24,26,31] Conversely, the four-electrode setup eliminates electrode polarization by decoupling the voltage and current sensing paths, enabling accurate measurements at lower frequencies, although being more susceptible to artifacts in the mid-to-high frequency region.[31] Conductivity was therefore evaluated in different frequency ranges: 320 to 500 kHz for the two-electrode measurement and from 0.5 to 2 kHz in the four-electrode configuration.

Impedance data were processed following the steps illustrated in Fig. 2(b). Since electrolytic conductivity is sensitive to temperature, only datapoints recorded after thermal equilibrium were included in further analysis. Within the selected frequency ranges, the real-valued conductivity was calculated *via* $\sigma'(\omega) = K_c \mathrm{Re}(Z(\omega)^{-1})$,[32] where $\omega = 2\pi f$ is the radial frequency, $Z(\omega)$ the recorded impedance, and K_c the electrical cell constant. The value of the latter was determined by calibration with a conductivity standard (Section S4.1, SI). Notably, the exact value of K_c is inconsequential in the context of crystallization monitoring, as only relative changes in conductivity are considered. To enable comparison of crystallization kinetics derived from impedance and X-ray data, all conductivity data were normalized using a previously reported strategy,[16,33] resulting in consistent profiles in the selected frequency ranges (Fig. S4, SI).

Powder X-ray diffraction (PXRD) was conducted using a monochromatic parallel X-ray beam at 25.05 keV (λ = 0.49537 Å) with a spot size of 500 × 500 μm^2 at the centre of the capillary. Diffraction data were collected using a Pilatus3 X 2M positioned 56.3 cm radially from the capillary centre, covering a q-range of 0.3–6.4 Å^{-1}.[34] The exposure time was set to 25 s in all experiments. Since the area under the Bragg reflections correlates to the volume of the crystals in the sample, evolution of the powder patterns can, similarly to conductivity, be used for kinetics measurements. The corresponding data processing steps are illustrated in Fig. 2(c), following a previously established procedure.[22] The final crystallization profiles were normalized, enabling direct comparison to the profiles derived from impedance data (Section S5, SI).

Fig. 3(a) and (c) presents the crystallization profiles from the different methods. In the pure Cs-based system, all techniques reveal highly consistent sigmoidal crystallization profiles, in line with prior studies of similar systems.[16,22] By comparison of the last pattern of the time series with a reference, the product was identified as phase-pure pollucite (R050344, **https://www.rruff.info**). Notably, profiles derived from conductivity show an earlier onset of crystallization than those derived from X-ray diffraction, pointing to higher sensitivity of the method to early-stage crystallization. This is consistent with the inherent limitations of powder XRD, which requires the presence of sufficiently large and well-ordered crystalline domains to generate detectable Bragg reflections. In the present crystallization system, the presence of Cs^+ promotes high nucleation rates, resulting in the initial formation of numerous small crystallites,[16] below the detection limit of XRD. After the main crystallization around t = 15 min, noticeable divergence between the profiles derived from impedance and X-ray characterization was observed. This results from the difference in what is observed: impedance indirectly monitors crystallization *via* changes in the ionic speciation in the mother liquor, where, in the case of alkaline zeolite formation, highly mobile hydroxide ions are generated upon the formation of new bonds between crystal growth units. This conversion of low- to high-mobility ions results in a conductivity increase. X-ray diffraction, on the other hand, directly probes long-range order in the crystalline phase. This means that, besides the crystallized

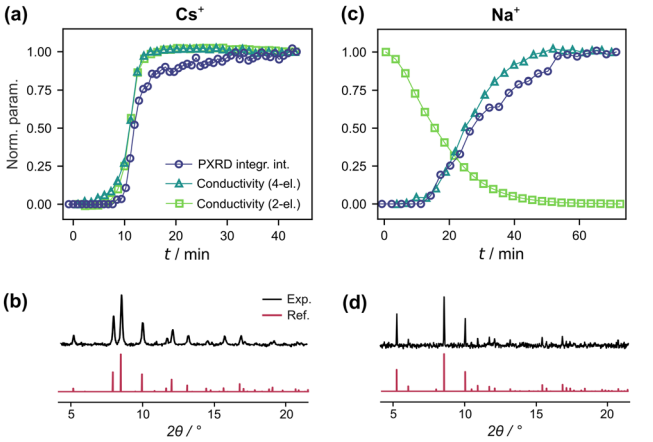

Fig. 3 (a) and (c) Comparison of crystallization profiles obtained from two- and four-electrode conductivity data, as well as from the integrated intensities of the PXRD patterns. (b) and (d) PXRD patterns at the end of the synthesis compared to reference data, confirming that the products are phase-pure pollucite and analcime for the Cs- and Na-based samples, respectively (R050344 and R040128; **https://www.rruff.info**). Evolution of PXRD patterns including the results of the peak fitting provided in Fig. S5.3 of the SI. Labels in the plots on the left apply also to those on the right.

volume, other factors, including Ostwald ripening or other aging-related processes, such as the healing of crystal defects, can contribute to the shape of diffraction lines. In addition to differences in the general shape of the profiles, a slight temporal shift is observed when comparing the crystallization half-times. This shift is attributed to two factors: the slower acquisition time of X-ray data (25 s) compared to impedance measurements (<0.5 s per frequency), and more importantly, axial temperature gradients caused by heater openings for optical access. These gradients result in slightly higher temperatures near the electrodes, promoting faster crystallization there compared to the centre of the capillary. Since WAXS probes only a 500 μm × 500 μm central region, while impedance integrates over the entire volume between the electrodes, the time shift and later differences in crystallization profiles may also partially arise from the spatial mismatch in measurement location combined with local temperature differences. Further investigation is still required to fully elucidate the differences observed between diffraction and impedance data.

Crystallization profiles for the Na system are shown in Fig. 3(c). Comparison of X-ray data to a reference[35] confirms that the product is phase-pure analcime (R040128, **https://www.rruff.info**). While both pollucite and analcime share the same zeolite framework type (ANA), Na^+ ions reside on more and different sites as compared to Cs^+. The narrower Bragg reflections for the Na-system as compared to the Cs-system indicate the formation of larger crystallites in the Na case. Similar to the Cs system, crystallization profiles obtained from PXRD and four-electrode impedance measurements in the Na system exhibit highly consistent behaviour throughout the entire crystallization process. In contrast, conductivity determined from the two-electrode measurement displays a markedly different trend, showing a declining signal for the latter. This

indicates pronounced reactions at the electrode–sample interface, presumably zeolitic depositions. These deposits locally increase the electrical resistance, thereby increasing the overall resistance measured in the two-electrode configuration. While this suggests a way to monitor crystallization on a metallic substrate, it prevents reliable *in situ* measurement of crystallization processes in the bulk. In the four-electrode approach, however, negligible current passes through the sensing electrodes, effectively eliminating such electrode-related artefacts,[24–27] similar to what was previously achieved using a differential impedance spectroscopy approach.[24,26,31]

Using an *in situ* zeolite crystallization study as an example, this work demonstrates the value of combining electrical and structural characterization within a single sample environment. In systems with high nucleation rates and small crystallites, impedance measurements sensitively detect early-stage processes, preceding the appearance of PXRD Bragg reflections. Combining two- and four-electrode methods distinguishes bulk from interfacial crystallization: the two-electrode setup captures interfacial effects, while the four-electrode configuration, unaffected by reactions at the electrode–sample interfaces, tracks bulk crystallization in agreement with PXRD-derived kinetics. Sensitivity arises from changes in ion mobility or speciation during crystallization, demonstrated for zeolite-crystallizing samples, where bond formation is accompanied by the release of highly mobile hydroxide ions. It is anticipated that the approach is broadly applicable to systems where phase evolution involves changes in ion speciation, mobility, or charge transport.

The authors acknowledge funding from FWO (12ACX25N, G083318N, and G0AC524N) and FWF (10.55776/I3680 and 10.55776/I6800). This work was further supported by KU Leuven (SiONA, C14/22/099). NMRCoRe is supported by the Flemish Government as an international research infrastructure (I001321N), and by Department EWI *via* the Hermes Fund (AH.2016.134). All authors acknowledge the European Synchrotron Radiation Facility (ESRF) for providing synchrotron radiation facilities under proposal numbers CH-7313 & IH-MA-605 and thank Vadim Diadkin for assistance and support in using beamline BM01.

Conflicts of interest

There are no conflicts to declare.

Data availability

The data supporting this article can be found in the SI. See DOI: **https://doi.org/10.1039/d5cc03808a**

Replication data are provided at Harvard Dataverse. See **https://doi.org/10.7910/DVN/S2P6WW**.

Notes and references

1 G. C. Halford, S. P. McDarby, S. Hertle, A. F. Kiely, J. T. Luu, C. J. Wang and M. L. Personick, *Nanoscale*, 2024, **16**, 11038–11051.
2 A. Roy, C. P. Healey, N. E. Larm, P. Ishtaweera, M. Roca and G. A. Baker, *ACS Nanosci. Au*, 2024, **4**, 176–193.
3 L. M. Liz-Marzán, C. R. Kagan and J. E. Millstone, *ACS Nano*, 2020, **14**, 6359–6361.
4 R. E. Abutbul and Y. Golan, *Nanotechnology*, 2020, **32**, 102001.
5 E. N. Lang and S. A. Claridge, *Nanotechnology*, 2021, **33**, 082501.
6 J. Hernández-Fernández, R. Vivas-Reyes and C. A. T. Toloza, *Int. J. Mol. Sci.*, 2022, **23**, 12148.
7 E. B. Kim, K. M. Tomczak, H. B. Chandrasiri, M. Pálmai, A. Ghaznavi, D. Gritsenko, J. Xu and P. T. Snee, *Front. Nanotechnol.*, 2023, **4**, 1096267.
8 E. Gomar-Nadal, B. R. Conrad, W. G. Cullen and E. D. Willams, *J. Phys. Chem. C*, 2008, **112**, 5646–5650.
9 D. Murzalinov, E. Dmitriyeva, I. Lebedev, E. A. Bondar, A. I. Fedosimova and A. Kemelbekova, *Processes*, 2022, **10**, 1116.
10 A. J. Mallette, J. T. Reiser, G. Mpourmpakis, R. K. Motkuri, J. J. Neeway and J. D. Rimer, *npj Mater. Degrad.*, 2023, **7**, 1–7.
11 K. Asselman, D. Vandenabeele, N. Pellens, N. Doppelhammer, C. E. A. Kirschhock and E. Breynaert, *Chem. Mater.*, 2022, **34**, 11081–11092.
12 K. Seefeldt, J. Miller, F. Alvarez-Núñez and N. Rodríguez-Hornedo, *J. Pharm. Sci.*, 2007, **96**, 1147–1158.
13 C. X. Wang, M. Wang and X. Zhou, *Biomaterials*, 2003, **24**, 3069–3077.
14 A. Wurm, R. Soliman, J. G. P. Goossens, W. Bras and C. Schick, *J. Non-Cryst. Solids*, 2005, **351**, 2773–2779.
15 M. Marzantowicz, J. R. Dygas, F. Krok, A. Łasińska, Z. Florjańczyk, E. Zygadło-Monikowska and A. Affek, *Electrochim. Acta*, 2005, **50**, 3969–3977.
16 D. Vandenabeele, N. Doppelhammer, S. Radhakrishnan, V. Chandran C, B. Jakoby, C. Kirschhock and E. Breynaert, *Microporous Mesoporous Mater.*, 2024, **374**, 113141.
17 K. Asselman, C. Kirschhock and E. Breynaert, *Acc. Chem. Res.*, 2023, **56**, 2391–2402.
18 V. Van Speybroeck, K. Hemelsoet, L. Joos, M. Waroquier, R. G. Bell and C. R. A. Catlow, *Chem. Soc. Rev.*, 2015, **44**, 7044–7111.
19 Y. Li, L. Li and J. Yu, *Chemistry*, 2017, **3**, 928–949.
20 C. J. Rhodes, *Sci. Prog.*, 2010, **93**, 223–284.
21 J. C. Jansen, *Advanced zeolite science and applications*, Elsevier, Amsterdam New York, 1994.
22 D. Vandenabeele, N. Doppelhammer, M. Rosenthal, W. Wangermez, B. Jakoby, C. Kirschhock and E. Breynaert, *J. Appl. Crystallogr.*, 2025, **58**(2), 392–397.
23 B. R. S. Hansen, K. T. Møller, M. Paskevicius, A.-C. Dippel, P. Walter, C. J. Webb, C. Pistidda, N. Bergemann, M. Dornheim, T. Klassen, J.-E. Jørgensen and T. R. Jensen, *J. Appl. Crystallogr.*, 2015, **48**, 1234–1241.
24 P. B. Ishai, M. S. Talary, A. Caduff, E. Levy and Y. Feldman, *Meas. Sci. Technol.*, 2013, **24**, 102001.
25 K. Asami, *Prog. Polym. Sci.*, 2002, **27**, 1617–1659.
26 C. Chassagne, E. Dubois, M. L. Jiménez, J. P. M. van der Ploeg and J. van Turnhout, *Front. Chem.*, 2016, **4**, 30.
27 U. Kaatze and Y. Feldman, *Meas. Sci. Technol.*, 2005, **17**, R17.
28 D. Vandenabeele, N. Doppelhammer, S. Radhakrishnan, C. V. Chandran, W. Wangermez, A. Rais, E. Vandeurzen, B. Jakoby, C. Kirschhock and E. Breynaert, *J. Mol. Liq.*, 2025, **417**, 126603.
29 L. Van Tendeloo, M. Haouas, J. A. Martens, C. E. A. Kirschhock, E. Breynaert and F. Taulelle, *Faraday Discuss.*, 2015, **179**, 437–449.
30 J. Vekeman, D. Vandenabeele, N. Doppelhammer, E. Vandeurzen, E. Breynaert, C. E. A. Kirschhock and T. Verstraelen, *Chem. Mater.*, 2024, **36**, 3886–3897.
31 N. Doppelhammer, T. Voglhuber-Brunnmaier, D. Vandenabeele, B. Jakoby and E. Breynaert, *Meas. Sci. Technol.*, 2024, **35**, 125501.
32 *Broadband Dielectric Spectroscopy*, ed., F. Kremer and A. Schönhals, Springer, Berlin, Heidelberg, 2003.
33 N. Doppelhammer, D. Vandenabeele, K. Asselman, E. Breynaert, B. Jakoby and C. E. A. Kirschhock, in 2023 International Workshop on Impedance Spectroscopy (IWIS), Chemnitz, Germany, 2023, pp. 51–55.
34 V. Dyadkin, P. Pattison, V. Dmitriev and D. Chernyshov, *J. Synchrotron Radiat.*, 2016, **23**, 825–829.
35 C. Baerlocher, D. Brouwer, B. Marler and L. B. McCusker, *Database of Zeolite Structures*, **https://www.iza-structure.org/databases/**, (accessed July 3, 2025).

